ACS APPLIED MATERIALS & INTERFACES

Research Article

www.acsami.org

# Effect of pH-Responsive Alginate/Chitosan Multilayers Coating on Delivery Efficiency, Cellular Uptake and Biodistribution of Mesoporous Silica Nanoparticles Based Nanocarriers

Wei Feng,[†,‡,§] Wei Nie,[†,§] Chuanglong He,[*,†,‡] Xiaojun Zhou,[‡] Liang Chen,[†] Kexin Qiu,[‡] Weizhong Wang,[†] and Zhiqi Yin[†]

[†]College of Chemistry, Chemical Engineering and Biotechnology, Donghua University, Shanghai 201620, China

[‡]Key Laboratory for Modification of Chemical Fibers and Polymer Materials, Donghua University, Shanghai 201620, China

Supporting Information

**ABSTRACT:** Surface fuctionalization plays a crucial role in developing efficient nanoparticulate drug-delivery systems by improving their therapeutic efficacy and minimizing adverse effects. Here we propose a simple layer-by-layer self-assembly technique capable of constructing mesoporous silica nanoparticles (MSNs) into a pH-responsive drug delivery system with enhanced efficacy and biocompatibility. In this system, biocompatible polyelectrolyte multilayers of alginate/chitosan were assembled on MSN's surface to achieve pH-responsive nanocarriers. The functionalized MSNs exhibited improved blood compatibility over the bare MSNs in terms of low hemolytic and cytotoxic activity against human red blood cells. As a proof-of-concept, the anticancer drug doxorubicin (DOX) was loaded into nanocarriers to evaluate their use for the pH-responsive drug release both *in vitro* and *in vivo*. The DOX release from nanocarriers was pH dependent, and the release rate was much faster at lower pH than that of at higher pH. The *in vitro* evaluation on HeLa cells showed that the DOX-loaded nanocarriers provided a sustained intracellular DOX release and a prolonged DOX accumulation in the nucleus, thus resulting in a prolonged therapeutic efficacy. In addition, the pharmacokinetic and biodistribution studies in healthy rats showed that DOX-loaded nanocarriers had longer systemic circulation time and slower plasma elimination rate than free DOX. The histological results also revealed that the nanocarriers had good tissue compatibility. Thus, the biocompatible multilayers functionalized MSNs hold the substantial potential to be further developed as effective and safe drug-delivery carriers.

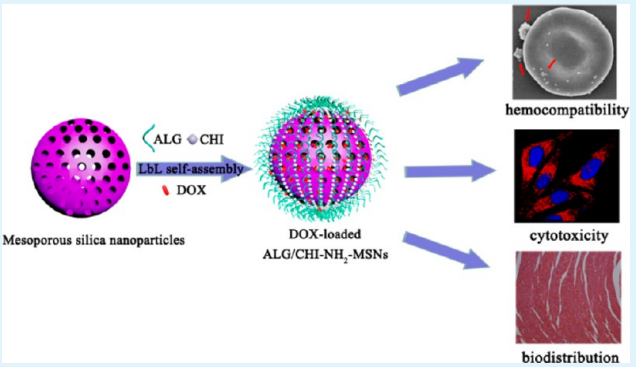


**KEYWORDS:** *mesoporous silica nanoparticles, layer-by-layer assembly, polyelectrolyte multilayer, pH-responsive, drug delivery*

## 1. INTRODUCTION

After over a decade of booming development, mesoporous silica nanoparticles (MSNs) have been recognized as one of the most promising biomedical platforms for therapeutic, diagnostic, prognostic, and combinatorial applications.[1,2] Benefiting from their stable mesoporous structures, large surface area, tunable pore size, easy surface functionalization, and good biocompatibility, MSNs can not only be fine-tuned to achieve the desired physicochemical characteristics for accommodating multiple cargo molecules such as therapeutic drugs, proteins, genes, and imaging agents either alone or in combination but also be engineered to facilitate the on-demand drug release and multimodality imaging.[3−5] Moreover, the newly emerged design features and synthetic schemes allow for integrating the robust therapeutic and diagnostic functions in a single all-in-one MSN platform. In such a theranostic system, therapeutic drugs can be precisely released to the target site, and the encapsulated imaging agents simultaneously provide the real-time noninvasive monitoring of biological responses to the therapy, thus enhancing the therapeutic efficacy.[4,6]

For these promises to be realized, however, the safety and efficacy issues related to the use of MSN-based nanocarriers in biomedical applications must be carefully addressed.[1,5,7] Many potential biomedical applications require intravenous administration, and hence these nanocarriers must guarantee a high degree of safety without producing adverse toxicity effects on human body. Additionally, for efficient *in vivo* drug delivery, nanocarriers should possess high drug loading efficiency, passive targeting by enhanced permeability and retention (EPR) effect, the ability to escape from the reticuloendothelial system (RES), a long blood circulation lifetime, and perfectly intelligent drug delivery capability. Surface functionalization is the most widely used way to render MSNs more biocompatible

**Received:** March 5, 2014
**Accepted:** April 21, 2014
**Published:** April 21, 2014

   dx.doi.org/10.1021/am501337s | *ACS Appl. Mater. Interfaces* 2014, 6, 8447−8460

by introducing bioactive moieties on the MSNs' surface. Previous studies have demonstrated that surface decoration with poly(ethylene glycol) (PEG) can impart MSN-based nanocarriers a desired stealth property, suppressing recognition and uptake by the RES and prolonging the circulation time *in vivo*.[8] Moreover, surface functionalization using specifically designed stimuli-responsive switches and/or targetable ligands as gatekeepers endow MSNs with the capabilities of controlled and/or targeted drug delivery. In these systems, the on-demand controlled release of encapsulated cargoes can be triggered in response to external or internal biological stimuli such as pH,[9,10] ultrasound,[11,12] temperature,[13,14] light,[15,16] redox,[17−19] magnetism,[20,21] electric-field,[22] and enzymes.[23,24] Among them, pH-responsive MSNs using pH-sensitive polymer coatings appeared as one of the most efficient therapeutic strategies in view of the fact that both cancerous tissues (pH 6.8) and endosomes/lysosomes (pH 5.5) are more acidic than normal tissues (pH 7.4).[25,26] So far, two main techniques including electrostatic layer-by-layer (LbL) self-assembly and surface radical polymerization were developed to obtain pH-sensitive polymer coatings on the MSNs surface.[27−29] The LbL technique has recently become a versatile method to assemble polyelectrolyte multilayer (PEM) films onto a number of substrates, allowing for nanoscale control of thickness, compositions, and molecular organization of the coating films. Furthermore, the building blocks for constructing the coating films can be optimally selected so as to create stimuli-responsive surfaces and structures.[30−32] As such, the LbL technique can be developed as a promising method for engineering of MSNs with the specific stimuli-responsive capabilities for controlled drug release applications.

In a previous study,[29] we fabricated PEM functionalized MSNs by assembling different layers of poly(allylamine hydrochloride) and poly(styrenesulfonate) onto the MSNs surface and demonstrated that the layer numbers of PEM coating have significant effects on their release profiles and biocompatibility *in vitro* and *in vivo*. For practical drug delivery applications, however, the carrier materials should be biocompatible and biodegradable to minimize harmful side effects. Chitosan (CHI) and alginate (ALG) are biodegradable, biocompatible, and natural marine based polysaccharides.[33,34] Under the specific pH conditions, the negatively charged carboxylate acid groups of alginate can form ionic bonds with the positively charged amino groups of chitosan to create pH-sensitive polyelectrolyte complexes.[35,36] As a result, the alginate/chitosan complex has been applied to design pH-responsive drug delivery carriers.

Herein, we present a facile strategy for the synthesis of functionalized MSN-based nanocarriers with pH-responsive delivery behaviors and improved biosafety features. For this purpose, MSNs were synthesized and then LbL assembled with alginate/chitosan multilayers to act as pH-sensitive gatekeepers and biocompatible shell layers. To evaluate the surface effects on the blood compatibility of MSNs, the hemolytic activity and morphological development of the erythrocyte were investigated. Doxorubicin hydrochloride (DOX), a classic anticancer drug with fluorescent properties, was encapsulated into nanocarriers to assess the pH-responsive drug loading and releasing behaviors. The cytotoxicity effects, cellular uptake, and subcellular localization were also evaluated with HeLa cells (human cervical carcinoma). Furthermore, the *in vivo* pharmacokinetics and biodistribution of the DOX-loaded nanocarriers were studied after intravenous administration into healthy rats. Due to the chemical versatility, both alginate and chitosan in shell layers can be further reacted with multifunctional molecules such as thermoresponsive polymers and/or targeting ligands,[37−39] thus allowing construction of multiresponsive nanocarriers. We believe that this study will provide important information for the rational design of MSN-based nanocarriers with improved biological effects and stimuli-responsive drug delivery features.

## 2. EXPERIMENTAL SECTION

**2.1. Materials.** Tetraethyl orthosilicate (TEOS), cetyltrimethylammonium bromide (CTAB), 3-aminopropyltriethoxysilane (APTES), fluorescein5(6)-isothiocyanate (FITC), chitosan with a degree of N-deacetylation of 75−85% (medium molecular weight), alginate (sodium salt, 15−20 cP, 1% in $H_2O$), hematoxylin, and eosin (H&E) were purchased from Sigma-Aldrich (Shanghai) Trading Co., Ltd. (Shanghai, China). DOX ($M_w$ 580) was obtained from the Beijing Huafeng United Technology Co, Ltd. (Beijing, China). Fetal bovine serum (FBS), penicillin-streptomycin, trypsin, and Dulbecco's modified Eagle's medium (DMEM) were obtained from Gibco Life Technologies Co. (Grand Island, USA). Paraformaldehyde was purchased from Beijing Dingguo Changsheng Biotechnology Co., Ltd. (Beijing, China). 4′,6-Diamidino-2-phenylindole (DAPI) was purchased from Bestbio (Shanghai, China). All other chemicals were obtained from Sinopharm Chemical Reagent Co. Ltd. (Shanghai, China).

**2.2. Synthesis of MSNs and FITC-labeled MSNs.** For the synthesis of MSNs, the procedure was employed as follows.[10] Briefly, 1.82 g of CTAB and 3.0 g of $NH_4F$ were dissolved in 500 mL of distilled water, then heated to 80 °C and stirred vigorously for 1 h. A total of 9.0 mL of TEOS was subsequently added dropwise to the above solution. After the resulting solution was stirred for 2 h, the product was collected by centrifugation at 10 000 rpm for 15 min and washed thoroughly with water and ethanol. To remove the surfactants, the as-synthesized nanoparticles were suspended in a mixture of 200 mL of ethanol and 4 mL of hydrochloric acid (36%−38%), and the solution was refluxed three times at 80 °C for 12 h. Finally, the surfactant-free products were dried under a vacuum for further use.

To visualize the cellular uptake, MSNs were labeled by FITC using the protocol described as follows. First, FITC-conjugated APTES (FITC-APTES) was prepared by reacting 4 mg of FITC and 44 μL of APTES under dark conditions for 24 h. Then, green fluorescence FITC-labeled MSNs (FMSNs) were obtained by the addition of FITC-APTES, followed by TEOS addition through a co-condensation reaction as reported previously.[38,40] Afterward, the surfactant-free FMSNs were treated and collected by the same method as described above.

**2.3. Synthesis of Aminated MSNs and FMSNs.** The surface of MSNs or FMSNs was functionalized with amine groups by treatment with APTES.[41] Typically, MSNs or FMSNs powder was dispersed in toluene by sonication for 5 min, followed by APTES addition to the suspension. The molar ratio of the samples (calculated as $SiO_2$: APTES: toluene) were fixed at 5:1:500, and the suspension was refluxed at 125 °C for 24 h under a nitrogen atmosphere. After filtering from the solution, and washing with toluene and ethanol twice respectively, aminated MSNs or FMSNs were dried under a vacuum.

**2.4. PEM Functionalization.** PEM functionalized MSNs (PEM-MSNs or PEM-FMSNs) were obtained by alternately

coating alginate and chitosan on the surface of aminated MSNs or FMSNs. First, alginate was dissolved in 0.5 M NaCl solution, and the pH was adjusted to 3.0 with acetic acid. A total of 25 mL of alginate solution (2 mg/mL in 0.5 M NaCl) was added to the aminated MSNs or FMSNs suspension (2.0 wt %, 25 mL) and stirred at room temperature for 2 h. The particles were centrifuged at 8000 rpm for 10 min, washed, and suspended with 0.5 M NaCl solution. Then, 25 mL of chitosan solution (2 mg/mL) was added to the suspension and stirred for 2 h, then centrifuged, washed, and redispersed in 0.5 M NaCl solution. PEM-MSNs or PEM-FMSNs could thus be obtained by repeating the above operations alternately and consecutively. In this study, we aimed to develop monodisperse and sub-200-nm nanocarriers, which have been reported to have long circulation times in the blood.[42,43] In addition, a small number of coating layers on MSNs are favorable for decreasing the particle aggregation. Therefore, two bilayers of alginate/chitosan were coated onto the MSNs for conferring pH sensitivity to nanocarriers.

**2.5. DOX Loading and Release *in Vitro*.** DOX was dissolved in distilled water with a concentration of 2 mg/mL. A total of 0.2 g of PEM-MSNs was added to 20 mL of DOX solution in PBS at 25 °C. The suspension was stirred for 12 h under dark conditions, then the soaked nanoparticles were vacuumed at room temperature for 2 h. The DOX-loaded nanocarriers (DOX@PEM-MSNs) were collected by centrifugation at 8000 rpm for 10 min and washing three times with distilled water. The supernatant and the washing solutions were collected together to determine the DOX loading by high performance liquid chromatography (HPLC). The drug loading content and entrapment efficiency were calculated by the following equations:

$$\text{Loading content (\%)} = \frac{\text{Weight of drug in PEM} - \text{MSNs}}{\text{Weight of drug loaded PEM} - \text{MSNs}} \times 100\% \quad (1)$$

$$\text{Entrapment efficiency (\%)} = \frac{\text{Weight of drug in PEM} - \text{MSNs}}{\text{Initial weight of drug}} \times 100\% \quad (2)$$

For *in vitro* drug release, the DOX-loaded sample (15 mg) was dispersed in 1.5 mL of solution. The dispersion was then transferred into a dialysis bag (molecular weight cutoff: 7000 Da). Then, the dialysis bag was kept in 20 mL of 50 mM buffer with different pH values (pH 4.0 and 5.2, acetate buffer; pH 6.8, 7.4 and 8.0, phosphate buffer) and gently stirred at 100 rpm and 37 °C. At predetermined time intervals, 10 mL of the solution was withdrawn, and an equal volume of fresh medium was added to keep the volume constant. The amount of released DOX was analyzed by HPLC.

HPLC analyses were performed with a high-performance liquid chromatography system (Agilent 1100 Series, USA) connected to a Waters C18 column (4.6 × 250 mm, 5 μm). The mobile phase A was 2.28 g/L sodium dodecyl sulfate (SDS; adjust pH to 6.0 with phosphoric acid), while the mobile phase B was acetonitrile. The mixing ratio of the mobile phase A and B was 25:75 (v/v) at a flow rate of 1 mL/min, and the column temperature was 40 °C. The column effluent was monitored with a fluorescence detector set at an excitation wavelength of 480 nm and an emission wavelength of 580 nm, respectively.

**2.6. Characterization.** The morphology and structure were investigated by using a Hitachi S-4800 (Hitachi Ltd., Japan) field emission scanning electron microscope (FESEM) and a JEM-2100F (Jeol Ltd., Japan) transmission electron microscope (TEM). The particle size distributions and the polydispersity indices (PDI) were evaluated by dynamic light scattering (DLS) using a BI-200SM multiangle dynamic/static laser scattering instrument (Brookhaven, USA). The zeta potential measurements were performed on a Zetasizer Nano ZS apparatus (Malvern, UK). Fourier transform infrared spectroscopy (FTIR) spectra were performed by a Nexus 670 (Thermo Nicolet, USA) spectrometer using KBr pellets. XRD patterns were obtained by a D/MAX-2550PC (Rigaku Inc., Japan) diffractometer with the Cu K$\alpha$ radiation at 45 kV and 40 mA, over a 2$\theta$ range of 1−10°. Thermogravimetric analysis (TGA) was conducted under air flow (50 mL/min) from the room temperature to 900 °C with a ramp of 10 °C/min using a TG 209 F1 (Netzsch, Germany) analyzer. The Brunauer−Emmett−Teller (BET) and Barrett−Jyner−Halenda (BJH) measurements were carried out to examine the surface areas and average pore size distributions, respectively. Nitrogen adsorption/desorption isotherms were measured with a Micromeritics Tristar II analyzer (Micromeritics, USA).

**2.7. Hemolysis Assay.** Heparin-stabilized fresh human blood samples were kindly supplied by the Shanghai First People's Hospital (Shanghai, China). Human red blood cells (RBCs) were centrifuged at 3000 rpm for 10 min at 4 °C and further washed more than five times with PBS. The purified RBCs were diluted 10× with PBS buffer, and 300 μL of diluted RBCs suspension was then mixed with bare MSNs and PEM-MSNs suspensions in 1.2 mL of PBS at concentrations from 25 to 800 μg/mL. PBS and distilled water were used as negative and positive control, respectively. The mixture was vortexed and incubated at 37 °C for 3 h, followed by centrifugation at 3000 rpm for 3 min. A total of 100 μL of supernatant from the sample was transferred to a 96-well plate. The absorbance values of the supernatants at 570 nm were measured using a Multiskan MK3 microplate reader with 630 nm as the absorption reference wavelength. The percent hemolysis of RBCs in each sample was calculated as in the following equation:

$$\text{Hemolysis (\%)} = \frac{\text{Sample absorbance} - \text{negative control}}{\text{positive control} - \text{negative control}} \times 100\% \quad (3)$$

For FESEM observation, purified RBCs suspension was incubated with bare MSNs and PEM-MSNs suspensions (100 μg/mL) for 3 h. The treated samples were then fixed in 1% glutaraldehyde in PBS buffer at room temperature for 2 h, followed by postfixation with 1% osmium tetroxide in PBS for 1.5 h. Then cells were dehydrated with graded ethanol (50, 60, 70, 80, 90, and 100%) for 30 min each. The samples were dropped onto glass coverslips, vacuum-dried, sputter-coated with gold, and observed under a Hitachi S-4800 FESEM.

**2.8. Intracellular Uptake and Intracellular Distribution of Nanoparticles.** HeLa cells were obtained from Shanghai Institute of Cell Biology, Chinese Academy of Sciences (Shanghai, China). Cells were cultured in DMEM supplemented with 10% FBS, 100 U/mL penicillin, and 100 μg/mL streptomycin. The cells were kept in a humid atmosphere containing 5% $CO_2$ at 37 °C. The medium was changed every 2

days, and the cells were passaged by trypsinization before confluence.

The cellular uptake ability of nanoparticles was quantitatively measured by flow cytometry (FCM). HeLa cells were treated with free DOX or DOX@PEM-MSNs (DOX concentration at 0.5, 1, 2, and 4 $\mu$g/mL). After 2 h of incubation, the medium was totally taken out and cells were washed with PBS and trypsinized. The cells were collected and centrifuged at 2000 rpm, washed with PBS twice, and resuspended in 1 mL of PBS. Then cell suspensions were filtered through 400-mesh sieves and finally subjected to a FACSCalibur flow cytometry (Becton Dickinson, USA) equipped with an argon laser (488 nm) and analyzed with CellQuest software through the fluorescence channel 2 (FL2) for DOX.

For CLSM observation, HeLa cells ($10^5$ cells per dish) were seeded into 20 mm glass bottom culture dishes and incubated for 24 h. After that, the medium was removed and the cells were incubated with PEM-FMSNs, DOX@PEM-MSNs, or free DOX (DOX at 1 $\mu$g/mL) at 37 °C for specific time points. Then the HeLa cells were rinsed twice with PBS, fixed with 4% paraformaldehyde for 10 min at room temperature, and observed by using a Carl Zeiss LSM 700 confocal laser scanning microscope (CLSM).

To study the endocytosis of nanoparticles, HeLa cells were incubated with PEM-MSNs (5.62 $\mu$g/mL) for 24 h. After that, the cells were washed with PBS and centrifuged at 1500 rpm for 10 min. The supernatants were removed, and the cells were fixed in a 0.1 M PBS solution containing 2.5% glutaraldehyde at 4 °C for 2 h. Then they were washed three times with PBS (0.1 M, pH 7.2), post fixed in 1% osmium tetroxide solution for 1 h, washed with PBS, dehydrated in a graded series of ethanol, and embedded in epoxy resin. The resin was polymerized in the oven at 37 °C for 12 h, 45 °C for 12 h, and 60 °C for 48 h. Ultrathin sections of approximately 70 nm were cut by an ultramicotome and stained with 5% aqueous uranyl acetate and 2% aqueous lead citrate and then observed with a JEM-2100 TEM.

To determine the subcellular localization, HeLa cells were incubated with drug-containing serum-free medium (DOX at 1 $\mu$g/mL) for 8 h, and then further incubated with 50 nM LysoTracker Green DND-26 (Molecular Probes, Invitrogen, USA) for 10 min or 200 nM MitoTracker Green FM (Molecular Probes) for 45 min to visualize lysosomes or mitochondria, respectively. Confocal fluorescence imaging was performed with a CLSM.

**2.9. Cytotoxicity Assay against HeLa Cells.** The cytotoxicity of DOX@PEM-MSNs was evaluated by examining the viability of HeLa cells after the treatment of nanoparticles using the CCK-8 Kits. Briefly, HeLa cells ($10^4$ cells per well) were seeded in a 96-well plate and cultured for 24 h to allow cells to attach. Then the medium was changed with fresh medium (blank control) and the medium containing the free DOX, PEM-MSNs, or DOX@PEM-MSNs (DOX at 0.5, 1, 2, and 4 $\mu$g/mL) for 24 and 48 h. Then 10 $\mu$L of CCK-8 solution was added into each well. After cells were incubated for another 4 h, the absorbance at 450 nm was measured by using a microplate reader (MK3, Thermo, USA). The relative cell viability was expressed as $[OD]_{test}/[OD]_{control} \times 100\%$, and the average value was obtained from five parallel samples.

For confocal microscopy observations, HeLa cells ($10^5$ cells per dish) were seeded in 20 mm glass bottom culture dishes and incubated for 24 h. After that, the medium was removed, and the cells were treated with PEM-FMSNs, DOX@PEM-MSNs, and free DOX (DOX at 1 $\mu$g/mL) at 37 °C for 24 and 48 h. After being washed twice in PBS, cells were fixed with 4% paraformaldehyde for 5 min and stained with 200 $\mu$L DAPI for 20 min at room temperature. 3D fluorescence images were obtained at a resolution of 512 × 512 pixels and a working distance of 180 $\mu$m. The Z-stack images were acquired from the fixed samples using 1.0 $\mu$m optical sections and were reconstructed to a 3D image for visualization using the ZEN Light Edition software (Carl Zeiss LSM 700, Germany).

**2.10. *In Vivo* Biodistribution of DOX in Rats.** All animal experiments were performed in compliance with the protocols approved by the Institutional Animal Care and Use Committees (IACUC) guidelines. Three-month-old male Sprague−Dawley (SD) rats (500−600 g; purchased from Shanghai Slac Laboratory Animal Co., Ltd., Shanghai, China) were kept under standard laboratory conditions with free access to complete food and water. All animals were acclimated to the animal facility for at least 7 days prior to experimental procedures.

For pharmacokinetic measurements, a total of 12 rats were randomly divided into three groups ($n$ = 4) and intravenously injected from the tail vein with 200 $\mu$L of sterile saline suspension of free DOX or DOX@PEM-MSNs at 2 mg DOX/kg body weight. The blood (250 $\mu$L/sample) of all the rats was collected at certain time intervals and stored in heparin-coated centrifuge tubes. The plasma was separated by centrifugation at 4000 rpm for 10 min at 4 °C. The samples were precipitated by adding an equal volume of methanol and then centrifuged at 13 000 rpm for 10 min. The supernatants were collected for DOX concentration quantification using a HPLC, as described above. Pharmacokinetic parameters were analyzed using Phoenix WinNonlin 6.3 software: $C_{max}$ = calculated maximum plasma concentration; $T_{max}$ = time of maximum plasma concentration; and $AUC_{0-\infty}$ = area under the concentration time curve from zero to $\infty$ with extrapolation of the terminal phase.

For quantitative analysis, the biodistribution of DOX and nanoparticles in the major organs, rats were assigned into three groups ($n$ = 3), including control, free DOX, and DOX@PEM-MSNs groups. The experimental groups were intravenously injected with 200 $\mu$L of sterile saline suspensions of free DOX and DOX@PEM-MSNs at the dose of 2 mg DOX/kg. Injections of sterile saline at equivalent volumes were given to rats as a control. Rats were sacrificed at 2 and 24 h after injection, and the following tissues were collected and weighed: heart, liver, spleen, lung, kidney, brain, and testis. Then, PBS solution was added to each tissue sample by an equal volume to its weight. After high speed homogenization, mixtures were centrifuged at 10 000 rpm for 10 min. The supernatant was collected and extracted with 4 times volume of chloroform/methanol (4:1, v/v) for 0.5 h. The obtained solution was transferred to a 1.5 mL centrifuge tube and evaporated in a gentle nitrogen flow at room temperature. The dry residues from tissues were reconstituted in 100 $\mu$L of methanol, and the amount of DOX in each tissue was analyzed by HPLC.

**2.11. Histological Examination.** The histological examinations were performed using standard laboratory procedures. The major organ samples excised from necropsy, including heart, liver, spleen, lung, kidney, brain, and testis, were collected and immediately fixed in 10% formalin in PBS solution. The organs were embedded in paraffin, sectioned into 4 $\mu$m sections, and then placed onto the glass slides. The histology

sections were stained with H&E and observed under a light microscope (Olympus, BH-2).

**2.12. Statistical Analysis.** All experiments were conducted at least three times, and all results were reported as the mean ± standard deviation (SD). Statistical analysis was carried out by the one-way analysis of variance (one-way ANOVA) and Scheffe's post hoc test. The statistical significance for all tests were at $*P < 0.05$ and $**P < 0.01$.

## 3. RESULTS AND DISCUSSION

**3.1. Synthesis and Characterization of PEM-MSNs.** The schematic fabrication process of DOX@PEM-MSNs is shown in Scheme 1. MSNs were synthesized and served as cores around which the alginate/chitosan multilayers were alternatively assembled via LbL technique. DOX was then trapped into the mesoporous channels and stayed inside the polymer shells. We hypothesize that the alginate/chitosan multilayers deposited around MSNs will not only act as pH-sensitive gatekeepers ensuring release of drug molecules in acidic conditions but also provide better biocompatibility for practical drug delivery applications.

**Scheme 1. Schematic Illustration for the Construction of pH-Responsive MSN-Based Nanocarriers and Intracellular pH-Triggered DOX Release**[a]

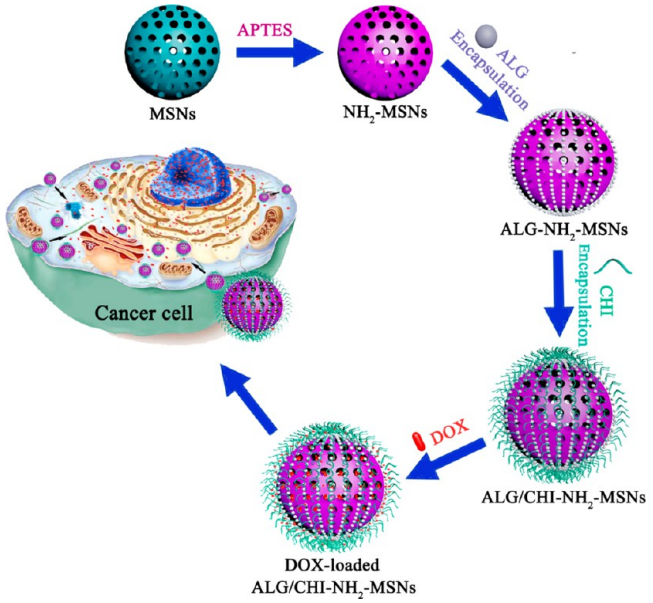


[a]Polyelectrolyte multilayers of alginate/chitosan (ALG/CHI) were alternatively deposited on the surface of aminated MSNs via LbL technique; DOX was then loaded into these nanocarriers. DOX release from these nanocarriers can be triggered by intracellular or external acidic environments.

SEM images showed that the pristine MSNs had a highly monodisperse spherical shape (Figure 1A), while PEM functionalization resulted in a slight aggregation of PEM-MSNs (Figure 1D). However, both nanoparticles exhibited good dispersity in aqueous solution (inset in Figure 1A and D). This was also supported by DLS measurements, where the measured hydrodynamic sizes were 110.2 nm for MSNs and 167.4 nm for PEM-MSNs with the corresponding PDI of 0.17 and 0.22, respectively (Figure 1C and F). TEM image (Figure 1B) clearly shows a partially ordered mesoporous structure within the MSNs. After being coated with two bilayers of alginate/chitosan, the thickness of the shell layer was confirmed to be around 25.5 nm by the TEM image (Figure 1F), which was slightly smaller than that determined by DLS (28.6 nm) due to the DLS technique measuring the hydrodynamic volume.

The surface functionalization of MSNs was further evaluated using FTIR, XRD, zeta potential measurement, TGA, BET, and BJH analyses (Figure S1, Supporting Information). The FTIR spectra (Figure S1A) showed the successful PEM functionalization of MSNs, which can be identified by several distinct peaks in the spectrum of PEM-MSNs. In the spectrum, MSNs showed the absorption of the Si−O−Si bond around 1030 $cm^{-1}$ and silanol bending vibration near 910 $cm^{-1}$. Apparently, the absorption band at 1580 $cm^{-1}$ can be assigned to the amino groups on the CHI. After deposition of CHI and ALG, the silanol absorption peak was weakened compared to bare MSNs. In addition, a newly broad peak emerged around 3340 $cm^{-1}$, which is attributed to the abundant hydroxyl (−OH) stretching vibration in ALG and CHI. The XRD pattern of MSNs (Figure S1B) exhibits a well resolved diffraction peak at around 2.0°, suggesting a partially ordered mesoporous structure. However, the diffraction peak almost disappeared in the pattern of PEM-MSNs, further confirming an effective coating. To monitor the coating process, the change of zeta potential was measured after different layers were coated. As shown in Figure S1C, the aminated MSNs have a positive surface charge of +17.5 mV due to the presence of the amino groups. The zeta potential changed between negative (up to −32.9 mV) and positive (up to +13.9 mV) values when alginate and chitosan were alternately coated on the MSNs surfaces. The overall amount of coated polymer can be quantified by TGA. As shown in Figure S1D, the weight loss values of MSNs and PEM-MSNs were 27.2% and 46.2%, respectively, when the temperature was increased to 900 °C. Therefore, the amount of coated polymer on the silica surface was calculated to be 26.1%. The surface area and porous nature of MSNs and PEM-MSNs were characterized by $N_2$ desorption/desorption measurements. The isotherm of MSNs (Figure S1E) shows a type IV curve of typical mesoporous material with a specific surface area of 167.4 $m^2/g$ and an average pore diameter of 5.7 nm (inset in Figure S1E). After surface functionalization, the surface area of PEM-MSNs was reduced to 30.4 $m^2/g$. This result indicated that most of the mesopores were obstructed by the polymer layers.

**3.2. Hemocompatibility of PEM-MSNs.** The hemocompatibility of nanoparticles is essential for their systemic administration as drug delivery carriers. Therefore, we evaluated the impacts of MSNs and PEM-MSNs on RBCs by using a hemolysis assay. As shown in Figure 2, bare MSNs exhibited dose-dependent hemolytic activity which increased rapidly with the increase of particle concentrations. The hemolysis percentage of bare MSNs reached 65.4 ± 3.4% at the particle concentration of 800 μg/mL, which is over 7-fold greater than the value 8.4 ± 1.3% at 100 μg/mL. In contrast, the PEM-MSNs exhibited a hemolysis percentage of lower than 1% even at the highest particle concentration tested. The results can also be evident from the optical images (inset in Figure 2) of blood samples where bare MSN-treated RBCs showed the leakage of hemoglobin into solution, but PEM-MSN-treated RBCs showed no visible hemolytic effects.

The interaction of particles with RBCs was further examined by SEM (Figure 3). When exposed to 100 μg/mL of bare MSNs, RBCs exhibited obvious morphological abnormalities


dx.doi.org/10.1021/am501337s | ACS Appl. Mater. Interfaces 2014, 6, 8447−8460

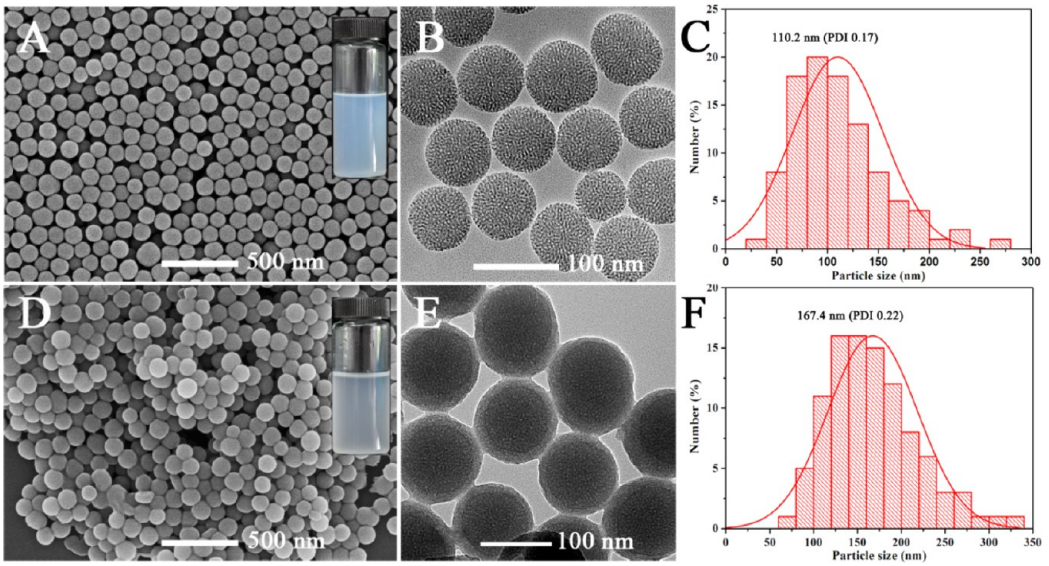


**Figure 1.** SEM images of (A) MSNs and (D) PEM-MSNs. The insets show that both the nanoparticles have good dispersity in aqueous solution. TEM images of (B) MSNs and (E) PEM-MSNs. Hydrodynamic size of (C) MSNs and (F) PEM-MSNs measured by the DLS method.

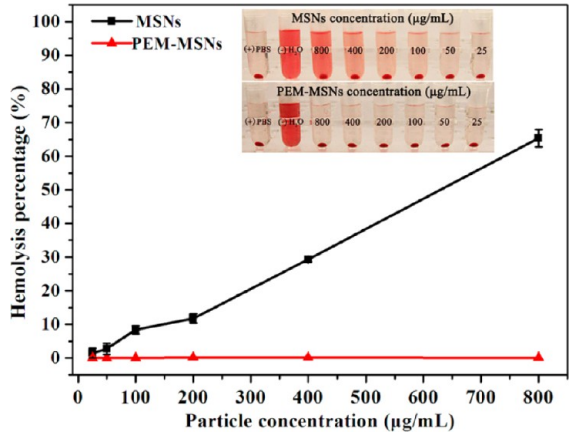


**Figure 2.** Hemolysis percentages of MSNs and PEM-MSNs at concentrations ranging from 25 to 800 $\mu$g/mL, which were incubated with human red blood cells (RBCs) at 37 °C for 3 h. The insets show the photographs of RBCs treated with MSNs and PEM-MSNs at different concentrations. PBS and distilled water were used as negative and positive controls, respectively.

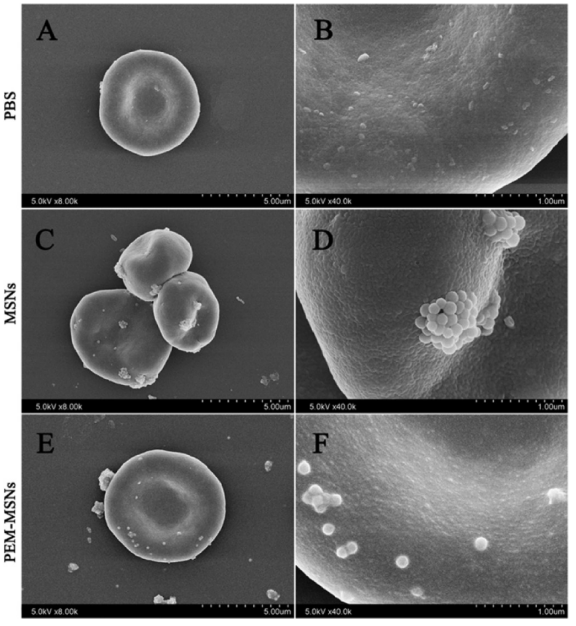


**Figure 3.** SEM images of RBCs incubated with (A) PBS, 100 $\mu$g/mL of (C) MSNs, and (E) PEM-MSNs suspension. (B, D, and F) Amplified images of A, C, and E, respectively. The nanoparticles attached on the cell surface are distinguished by the particle shape and surface textural difference between the particles and RBCs.

and progressive membrane destruction (Figure 3C and D) compared to control RBCs (Figure 3A and B). In contrast, PEM-MSN-treated RBCs (Figure 3E and F) maintained their normal biconcave disc shape similar to that of the untreated cells. The results indicate that PEM-MSNs have negligible hemolysis activity, which is possibly due to the surface silanol or amino groups of the nanoparticles being blocked by polymer layers, thus decreasing the affinity of the bare nanoparticles to RBCs membrane and in turn preserving the integrity of the RBCs membrane.[44]

**3.3. Drug Loading and *in Vitro* pH-Responsive Release.** To evaluate the drug loading and releasing property of MSN-based nanocarriers, DOX was loaded into the prepared PEM-MSNs. According to eqs 1 and 2, the drug loading content and entrapment efficiency were calculated as 15.1 ± 1.1% and 80.7 ± 4.2%, respectively. The drug release behaviors of the DOX@PEM-MSNs were assessed at 37 °C under different pH conditions. As Figure 4A shows, the release of DOX from nanocarriers was pH-dependent, and the release rate increased with the decrease of pH value. When alkaline (pH 8.0) and neutral (pH 7.4) release media were used, the amounts of released DOX from DOX@PEM-MSNs were only 5.2% and 7.5% over the total 132-h time period. The results suggest that the polymer shell is in a nearly closed state under alkaline or neutral conditions and thus blocks the pore outlets of MSNs and inhibits DOX release. However, when the release medium is acidic, the release rate obviously increases with the increase in the acidities of release medium. Throughout the entire time period, approximately 10.7%, 48.6%, and 60.1% of the entrapped DOX was released at pH 6.8, 5.2, and 4.0, respectively. The results are probably attributed to the


dx.doi.org/10.1021/am501337s | ACS Appl. Mater. Interfaces 2014, 6, 8447−8460

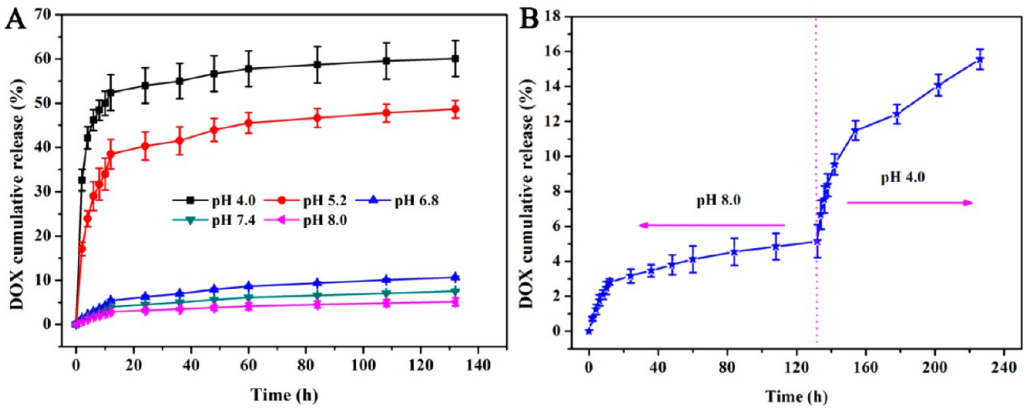


**Figure 4.** (A) Release profiles of DOX from DOX@PEM-MSNs at different pH values. (B) pH-controlled release of DOX from DOX@PEM-MSNs.

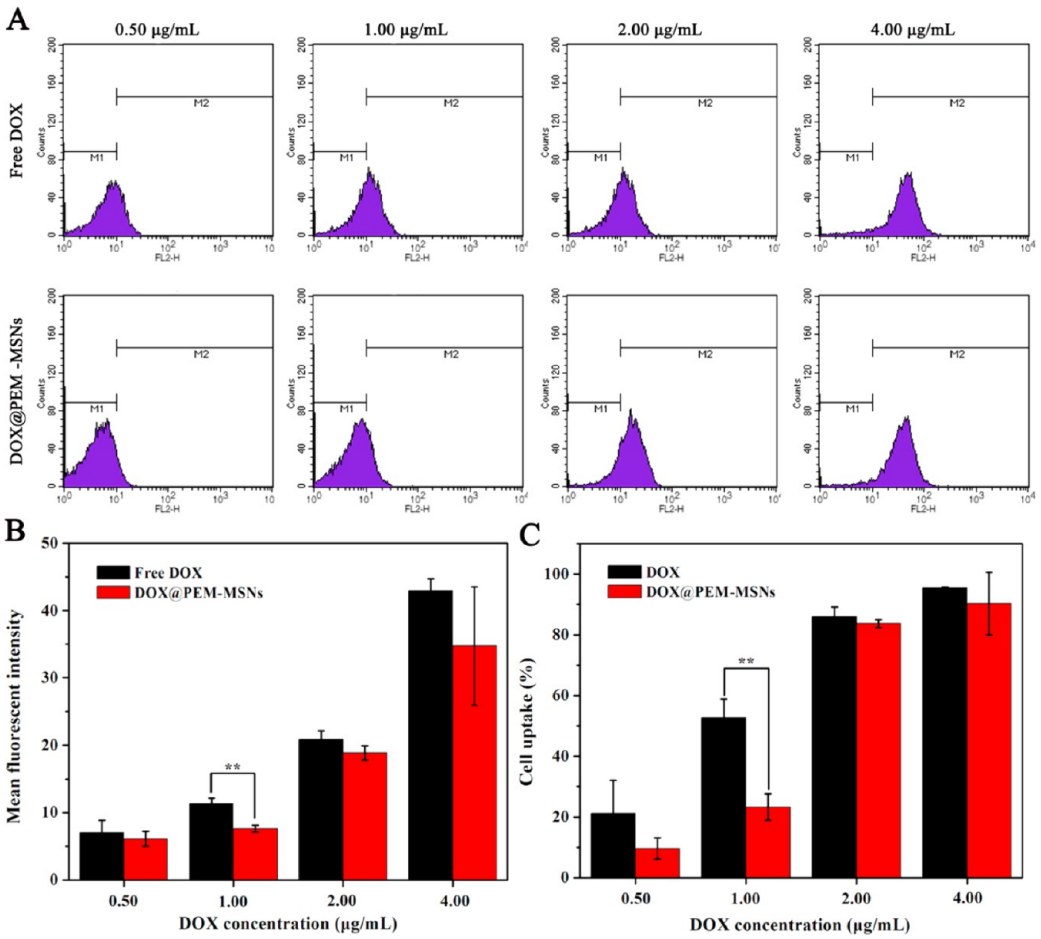


**Figure 5.** *In vitro* cellular uptake of free DOX and DOX@PEM-MSNs against HeLa cells. (A) Flow cytometry assays of cellular uptake, (B) mean fluorescence intensity, and (C) cellular uptake percentage of free DOX and DOX@PEM-MSNs at DOX concentrations ranging from 0.5 to 4 μg/mL. $^{**}p < 0.01$ compared with free DOX group.

electrostatic repulsion between the DOX molecules and the ionized amino groups (from aminated MSNs and chitosan), the disruption of alginate/DOX ionic complexes, and the large concentration gradient between nanocarriers and bulk solution. At lower pH values, the amino groups on $NH_2$-MSNs and chitosan become progressively ionized; the increased electrostatic repulsion between the DOX molecules and the ionized amino groups may cause a rapid drug release. Concurrently, the carboxylate groups on alginate become less negatively charged at lower pH, which would reduce the electrostatic attraction between alginate and DOX and results in increased DOX release.[45] As the $pK_a$ of DOX is 8.2, lower pH value leads to higher solubility of DOX[46] and a larger concentration gradient between nanocarriers and bulk solution, which also causes increased drug release. In addition, successive exposure of DOX@PEM-MSNs to different release media at pH 8.0 and 4.0 resulted in a pH-dependent "off" and "on" switching of DOX release (Figure 4B). As such, the prepared DOX@PEM-MSNs


dx.doi.org/10.1021/am501337s | ACS Appl. Mater. Interfaces 2014, 6, 8447−8460

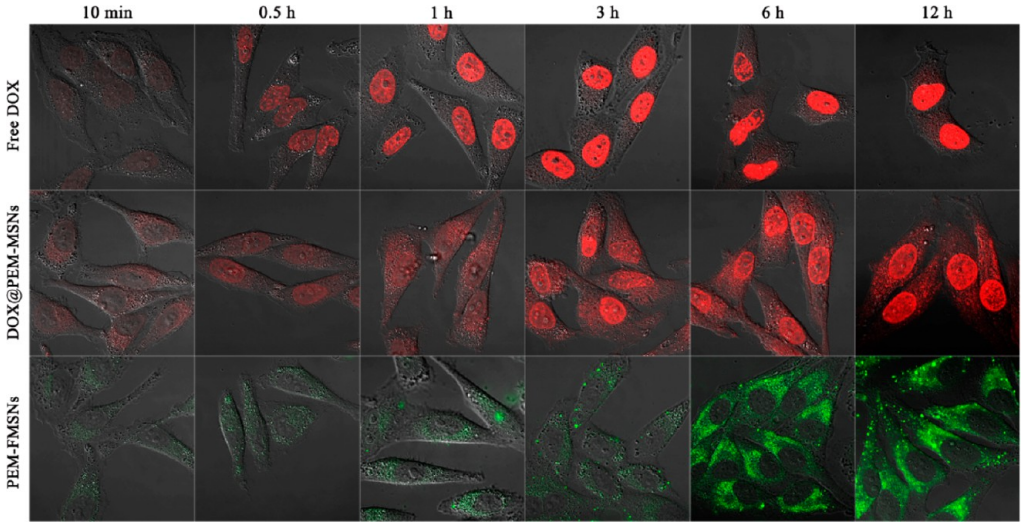


**Figure 6.** Confocal laser scanning microscopy (CLSM) images of HeLa cells treated with free DOX, DOX@PEM-MSNs, and PEM-FMSNs at DOX concentration of 1 $\mu$g/mL and 37 °C for different time periods. The red fluorescence represents the released DOX or DOX@PEM-MSNs, and the green fluorescence represents the PEM-FMSNs. Cells were imaged using a 63× oil-immersion objective.

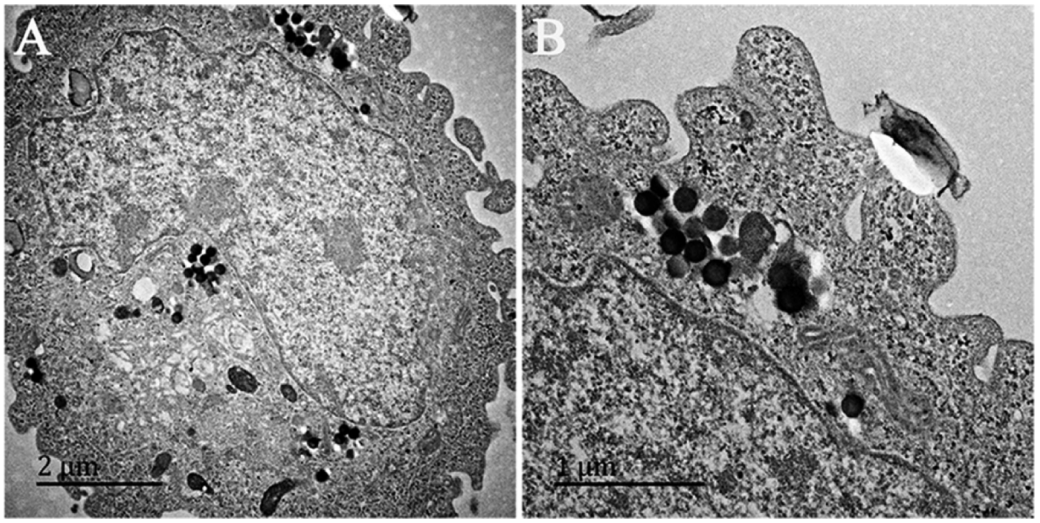


**Figure 7.** (A) TEM images of the uptake and subcellular localization of PEM-MSNs in HeLa cells. (B) Magnified image of A. The images show that the abundant PEM-MSNs are internalized into cells and mainly accumulated in the perinuclear region, and some nanoparticles are trapped into the intracellular endosomes/lysosomes.

may be further developed as a pH-responsive release system that can target tumor cells and allow drug release within acidic intracellular compartments such as endosome and lysosome, where the pH value is lower than that in the normal tissue.

### 3.4. Cellular Uptake and Intracellular Release of DOX.

The cellular uptake of DOX in HeLa cells was quantified using flow cytometry via the inherent red fluorescence signal of DOX after cells were treated with free DOX or DOX@PEM-MSNs at DOX concentration of 0.5−4 $\mu$g/mL for 2 h. As shown in Figure 5A and B, the mean fluorescence intensity increased with the increase of equivalent concentration of DOX for both formulations. At the same equivalent DOX concentration, free DOX did not produce a significant increase in fluorescence intensity when compared to the DOX@PEM-MSNs group, except at the DOX concentration of 1 $\mu$g/mL ($p < 0.01$; Figure 5B). The percent population of cells uptaken with DOX was also used to evaluate the cellular uptake of DOX-loaded nanocarriers (Figure 5C). At the same DOX concentration, although somewhat higher uptake efficiency was found in HeLa cells after treatment with free DOX compared with DOX@PEM-MSNs, no significant cell population difference was observed except at the DOX concentration of 1 $\mu$g/mL ($p < 0.01$). The results indicate that PEM-MSNs can be used as effective carriers for delivering therapeutic drugs into cells with high uptake efficiency, and their uptake efficiency may be further improved after the incorporation of target-specific ligands.

Effective cell internalization of nanocarriers plays a vital role in the delivery of cargo molecules to the right destination. We investigated the internalization and intracellular drug release behaviors of nanocarriers by CLSM, after incubation of free DOX, DOX@PEM-MSNs, and FITC-labeled nanocarriers (PEM-FMSNs) with HeLa cells for different time intervals. As shown in Figure 6, the intracellular DOX delivery from both the DOX formulations exhibited the similar profiles in HeLa cells but at different time points. Free DOX can easily and

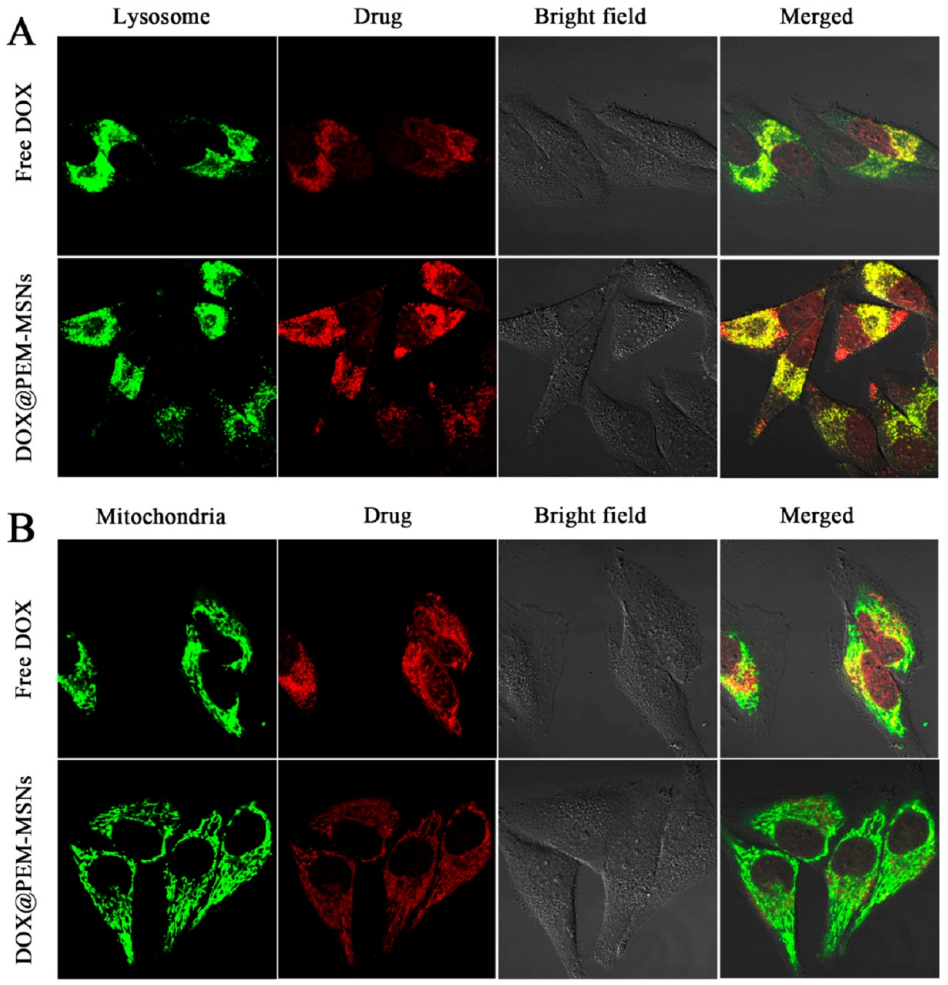


**Figure 8.** Intracellular distributions of free DOX and DOX@PEM-MSNs in HeLa cells, which were incubated with DOX and DOX@PEM-MSNs at a DOX concentration of 1 $\mu$g/mL and 37 °C for 8 h, followed by treatment with organelle-selective dyes and observation by CLSM. (A) Free DOX (red) and DOX@PEM-MSNs (red) indicated the distribution of drug in HeLa cells with labeled lysosomes (green). (B) Free DOX (red) and DOX@PEM-MSNs (red) indicated the distribution of drug in HeLa cells with labeled mitochondria (green), respectively. Cells were imaged using a 63× oil-immersion objective.

rapidly enter into HeLa cells and accumulates in the cell nuclei via diffusion within 10 min of incubation, and the intensive red fluoresence can be observed inside the cell nuclei after 30 min of incubation. For DOX@PEM-MSNs, however, the red fluoresence was initially located only in the perinuclear area of the cytoplasm after incubation for 10 min and then appeared and became more intense in the nucleus with increasing incubation time. The result demonstrated that the DOX-loaded nanocarriers need to be endocytosed into the cells and release the DOX within the cytosol, followed by diffusion into the nuclei, resulting in a slower and prolonged DOX accumulation in the nuclei.[47] In addition, the empty nanocarriers appear to be located only in the cytoplasm of HeLa cells. Only weak green fluorescence can be detected in the cytoplasm after incubation of 10 min, and the fluorescence intensity was gradually enhanced in the perinuclear region with the incubation time up to 12 h. No fluorescence was seen inside the nucleus. The endocytosis and the distribution of empty nanocarriers inside the HeLa cells can be further evidenced by TEM images. As shown in Figure 7, a number of nanoparticles were encapsulated into vesicular compartments, phagocytized by the cell, and trapped into the intracellular endosomes/lysosomes, and some of the internalized nanoparticles maintained their sphere morphology and were not surrounded by the membrane-like structures, suggesting that the nanoparticles might escape from the endosomes/lysosomes into the cytoplasm.[48] The above results revealed that empty nanocarriers can be uptaken by HeLa cells and localized in the cytoplasm rather than the nucleus.

To further clarify the intracellular distribution of DOX@PEM-MSNs, the lysosomal and mitochondrial compartments of HeLa cells were labled with green fluorescent lysotracker and mitotracker, respectively. After 8 h of incubation, the colocalization of green and red fluorescence revealed that DOX@PEM-MSNs were mainly localized in lysosomes (Figure 8A) and occasionally in the cytosol and mitochondria (Figure 8B). The CLSM images also revealed that free DOX was primarily localized in the cell nucleus and only a small number of them were released in the lysosomes and mitochondrias after 8 h of incubation (Figure 8).

Combined with all the above results, we conclude that free DOX and DOX-loaded nanocarriers might exploit different uptake mechanisms to enter HeLa cells. Since DOX is a small molecule drug, free DOX can readily diffuse through the cell membrane and rapidly enter the cell nucleus, whereas DOX-loaded nanocarriers are probably internalized into the cells

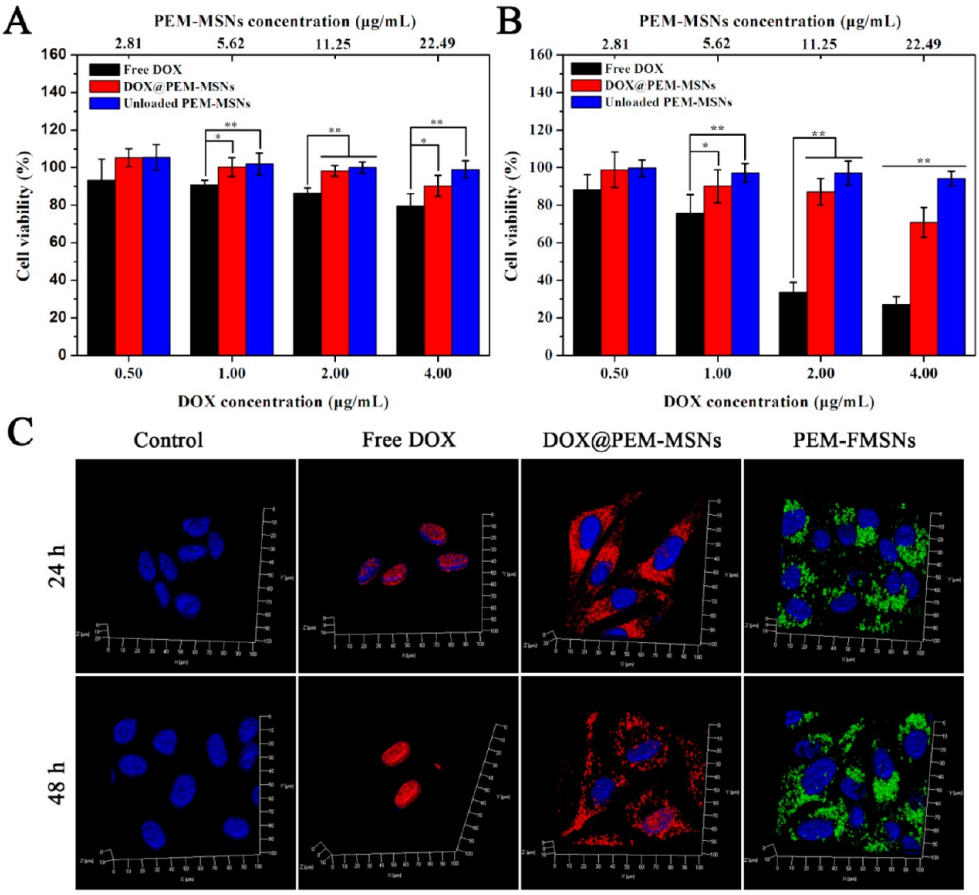


**Figure 9.** The cytotoxicity of free DOX, DOX@PEM-MSNs, and unloaded PEM-MSNs against HeLa cells incubated for (A) 24 h and (B) 48 h. (C) The 3D CLSM images of HeLa cells, which were incubated with blank medium, free DOX, DOX@PEM-MSNs, and PEM-FMSNs at a DOX concentration of 1 μg/mL and 37 °C for 24 and 48 h. DAPI was used for blue staining of the cell nuclei. Red fluorescence corresponds to the DOX (or DOX@PEM-MSNs). Green fluorescence represents PEM-FMSNs. Cells were imaged using a 63 × oil-immersion objective.

through clathrin- or caveolae-mediated endocytosis and are localized in endosomes/lysosomes.[49] As indicated by CLSM and TEM images, the empty nanocarriers were retained in the cytoplasm without entering the nucleus due to their large particle size. Afterward, the acidic environment of endosomes/lysosomes would trigger pH-dependent DOX release from the nanocarriers, and the endosomally released DOX would be subsequently translocated from the cytoplasm into the nucleus by proteasome-mediated mechanisms.[50] As a result, the DOX-loaded nanocarriers possess a sustained intracellular release profile that allows the prolonged DOX accumulation in the nucleus, thereby achieving decreased toxicity and prolonged therapeutic effectiveness.

**3.5. *In Vitro* Cytotoxicity Assay.** In order to evaluate the biological activity of the loaded DOX, the cytotoxic effects of free DOX, DOX-loaded nanocarriers, and empty nanocarriers against HeLa cells were assessed using the CCK-8 cell viability assay. The studies were conducted by incubation of HeLa cells with DOX@PEM-MSNs at DOX concentrations of 0.5, 1, 2, and 4 μg/mL (the relative concentration of PEM-MSNs were 2.8, 5.6, 11.3, and 22.5 μg/mL, respectively) for 24 and 48 h; the free DOX and empty PEM-MSNs containing a comparable amount of either DOX or nanocarriers were also examined for control and comparison. As can be seen from Figure 9A and B, empty PEM-MSNs showed no obvious cytotoxicity at any of the concentrations used even incubation for 48 h, which demonstrated that PEM-MSNs had excellent cytocompatibility as nanocarriers. In contrast, both free DOX and DOX@PEM-MSNs caused a dose-dependent increase in cytotoxicity at both incubation time points, and free DOX resulted in a significantly higher toxicity ($p < 0.05$) than DOX@PEM-MSNs when cells were exposed at the same DOX dose, except at a DOX concentration of 0.5 μg/mL where no significant difference was observed at both time points. This may be due to the fact that DOX molecules loaded in nanocarriers need to spend a longer period of time to enter into the nucleus than free DOX, resulting in an accumulated and prolonged cytotoxic effect. Furthermore, as expected, the increase in incubation time resulted in the enhanced cytotoxic effect for both DOX formulations with the same DOX concentrations. For instance, the cell viability of DOX@PEM-MSNs (DOX at 4 μg/mL) decreased from 90.3 ± 5.5% to 70.9 ± 7.9% when incubation time extended from 24 to 48 h.

The effect of different treatment conditions on cell viability was further investigated by using 2D CLSM images, which provided the visible evidence of cytotoxity after treated HeLa cells with two DOX formulations (DOX at 1 μg/mL) and empty nanocarriers for 24 and 48 h. As indicated in Figure S2, free DOX-treated cells displayed morphological features of apoptosis or necrosis including enlarged nucleus and collapsed cytoplasm after treatment for 24 h, and most cells exhibited the abnormal morphology with shrunk cytosol and rounded shape after being incubated with DOX@PEM-MSNs from 24 to 48 h. The cells treated with empty nanocarriers showed no obvious


dx.doi.org/10.1021/am501337s | ACS Appl. Mater. Interfaces 2014, 6, 8447−8460

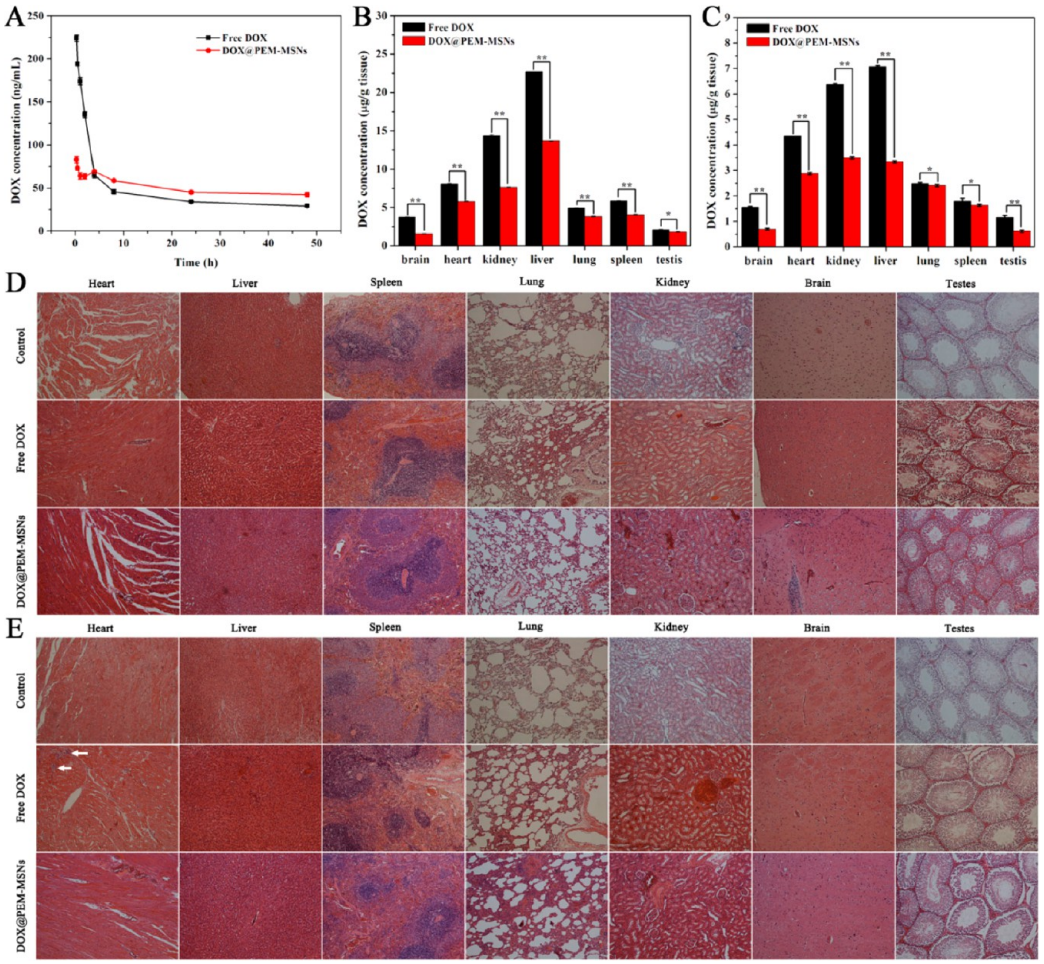


**Figure 10.** (A) Plasma concentration of DOX after intravenous administration with free DOX and DOX@PEM-MSNs at a dose of 2 mg DOX/kg. The biodistribution of DOX in healthy SD rats at (B) 2 h, (C) 24 h after intravenous administration of free DOX and DOX@PEM-MSNs at the dose of 2 mg DOX/kg. *$p < 0.05$ and **$p < 0.01$ compared with free a DOX group. Histological examination of major organs from the healthy SD rats intravenously administrated with saline, free DOX, and DOX@PEM-MSNs at (D) 2 h and (E) 24 h after injection. White arrows indicate the inflammatory cells infiltration in the heart. Images were 100× the original magnification.

abnormity on the morphology at different time periods, confirming that the cytotoxicity was due to the released DOX and not the nanocarriers. To precisely track and localize DOX and nanocarriers in HeLa cells, the reconstructed 3D CLSM images (Figure 9C) of the drug and nanocarrier-treated cells were created after incubation of cells for 24 and 48 h, where red, blue, and green represent the DOX, nuclei, and empty nanocarriers, respectively. As pictured in Figure 9C, free DOX can be directly entered inside the nucleus after 24 h and distributed over the whole nucleus within 48 h, thus resulting in a time-dependent cytotoxic effect. For DOX@PEM-MSNs treated HeLa cells, strong DOX fluorescence is primarily located in the perinuclear region of cells at the 24 h time point, and a more intense red fluorescence is observed in the nucleus at 48 h after incubation. In contrast, the green fluorescence of empty nanocarriers is found in the cytoplasm for 24 h and the fluorescence intensity continued to increase during the next 24 h. These results suggested that a fraction of the loaded DOX is still entrapped in the nanocarriers and retained in the cytoplasm even after 48 h of incubation, which may require a more extensive time period for translocating from plasma to nucleus. Consequently, it can be reasonably expected that the DOX-loaded PEM-MSNs would exert a more favorable long-term growth-inhibiting effect on the cells as compared with free DOX.

**3.6. *In Vivo* Pharmacokinetics, Biodistribution, and Histology Studies.** DOX concentration in rat plasma was tested after administration of free DOX and DOX@PEM-MSNs at different time points. The concentration−time curve is illustrated in Figure 10A, and the pharmacokinetic parameters are presented in Table 1. Statistically significant differences ($p < 0.01$) were found in the major pharmacokinetic parameters between both DOX formulations. Free DOX exhibited a biphasic and more rapid blood clearance compared

**Table 1. Pharmacokinetic Parameters of DOX after Intravenously Administration of Free DOX and DOX@PEM-MSNs to SD Rats at the DOX Dose of 2 mg/kg ($n = 4$)**

| parameter | DOX | DOX@PEM-MSNs |
|---|---|---|
| $C_{max}$ (μg/mL) | 0.22 | 0.08[a] |
| $T_{max}$ (h) | 0.30 | 0.30 |
| $T_{1/2}$ (h) | 64.80 ± 12.80 | 262.50 ± 33.60[a] |
| $AUC_{0-24}$ (μg h/mL) | 2.17 ± 0.08 | 3.02 ± 0.10[a] |
| $AUC_{0-\infty}$ (μg h/mL) | 4.90 ± 0.63 | 27.98 ± 5.09[a] |

[a]$p < 0.01$ compared with DOX.


dx.doi.org/10.1021/am501337s | ACS Appl. Mater. Interfaces 2014, 6, 8447−8460

with DOX@PEM-MSNs formulation, with a half-time ($t_{1/2}$) of 64.8 h and an area under the curve ($AUC_{0-\infty}$) of 4.9 $\mu$g h/mL. Whereas, DOX@PEM-MSNs displayed a relatively slow and steady DOX release than free DOX, giving a $t_{1/2}$ of 262.5 h and $AUC_{0-\infty}$ of 27.98 $\mu$g h/mL, which were 4.1 times longer and 5.7 times higher than free DOX, respectively. The results indicated that DOX-loaded nanocarriers had a longer systemic circulation time and slower plasma elimination rate compared to free DOX, which would increase the ability of nanocarriers to take advantage of the EPR effect for the accumulation of drugs in the desired site such as a tumor.

The concertrations of DOX in major organs were also measured after administration of free DOX and DOX@PEM-MSNs for 2 and 24 h. As shown in Figure 10B and C, DOX concentrations in all major organs were decreased for both DOX formulations from 2 to 24 h after injection, implying that DOX can be gradually eliminated in major organs with the time extending. At both time points, DOX-loaded nanocarriers showed statistically significant lower DOX accumulation in the major organs than free DOX, especially in the liver, kidney, and heart. The lower DOX acumulation in major organs might be attibuted to the prolonged circulation of DOX@PEM-MSNs in the bloodstream, which could help to reduce the cardiotoxicity due to high DOX accumulation in the heart.

Histological analysis of major organs was performed to investigate the *in vivo* toxicity of different DOX formulations. Figure 10D and E showed H&E stained hisological sections of the major organs of rats after injection with saline, free DOX, and DOX@PEM-MSNs for 2 and 24 h, respectively. Compared with the control group, a marked inflammatory cell infiltration was observed in the heart tissue of rats treated with free DOX for 24 h (Figure 10E), indicating acute cardiotoxicity produced by DOX. In contrast, no histological evidence for acute cardiotoxicity was perceived in the DOX@PEM-MSNs treated group. This indicated that the cardiotoxicity of DOX was alleviated when delivered by nanocarriers, probably due to a reduction in DOX accumulation in the heart. In addition, no acute pathological change was detected in all other organs, suggesting that the nanocarriers possess good tissue compatibility. Taking all of the *in vivo* results together, the developed nanocarriers are capable of releasing the drug in a slow and gradual manner, and thus decreased the drug accumulation in major organs, which could potentially maximize therapeutic effect with minimal toxicity to healthy tissues.

## 4. CONCLUSION

In summary, a pH-responsive MSN-based nanocarrier was fabricated by using MSNs as core and biocompatible polyelectrolyte multilayers of alginate/chitosan as a shell via the LbL technique. The assembled polymer shell not only provides the pH sensitivity and improved biocompatibility but also enables further funcationalization of MSNs with multifunctional ligands. Compared with bare MSNs, the functionalized MSNs exhibited significantly improved blood compatibility in terms of low hemolytic and cytotoxic activity against human RBCs, which make them promising candidates for intravascular drug delivery. As a proof-of-concept, we demonstrated their application for the pH-responsive release of the anticancer drug DOX both under *in vitro* and *in vivo* conditions. The *in vitro* evaluation indicated that the DOX-loaded nanocarriers exhibited a sustained intracellular DOX release and a prolonged DOX retention in the nucleus, thus showing a reduced toxicity and prolonged therapeutic efficacy, whereas the empty nanocarriers were retained in the cytoplasm and showed no cytotoxicity to HeLa cells. In addition, the pharmacokinetic and biodistribution studies in healthy rats showed that DOX-loaded nanocarriers had longer systemic circulation time and slower plasma elimination rate than free DOX. The histological results also revealed that DOX-loaded nanocarriers had good tissue compatibility. These results, coupled with the capacity to be functionalized with targeting ligands, make the PEM functionalized MSNs a promising nanocarrier for efficient and safe delivery of anticancer drugs and other therapeutic agents.

## ■ ASSOCIATED CONTENT

### Supporting Information

Characterization of the synthesized MSNs and PEM-MSNs and confocal laser scanning microscopy images of HeLa cells incubated with blank medium, free DOX, DOX@PEM-MSNs, and PEM-FMSNs. All of this information is available free of charge via the Internet at http://pubs.acs.org/.

## ■ AUTHOR INFORMATION

### Corresponding Author

*Tel./fax: +86 21 6779 2742. E-mail: hcl@dhu.edu.cn.

### Present Address

[§]Contributed equally to this work.

### Notes

The authors declare no competing financial interest.

## ■ ACKNOWLEDGMENTS

This study was financially supported by the National Natural Science Foundation of China (31271028), Shanghai Nano Science Program (11 nm0505500), Innovation Program of Shanghai Municipal Education Commission (13ZZ051), Chinese Universities Scientific Fund (CUSF-DH-D-2014035), and Open Foundation of State Key Laboratory for Modification of Chemical Fibers and Polymer Materials (LK1202).

## ■ REFERENCES

(1) Chen, Y.; Chen, H. R.; Shi, J. L. In Vivo Bio-Safety Evaluations and Diagnostic/Therapeutic Applications of Chemically Designed Mesoporous Silica Nanoparticles. *Adv. Mater.* **2013**, *25*, 3144−3176.

(2) Mamaeva, V.; Sahlgren, C.; Linden, M. Mesoporous Silica Nanoparticles in Medicine−Recent Advances. *Adv. Drug Delivery Rev.* **2013**, *65*, 689−702.

(3) Tang, L.; Cheng, J. J. Nonporous Silica Nanoparticles for Nanomedicine Application. *Nano Today* **2013**, *8*, 290−312.

(4) Chen, N. T.; Cheng, S. H.; Souris, J. S.; Chen, C. T.; Mou, C. Y.; Lo, L. W. Theranostic Applications of Mesoporous Silica Nanoparticles and Their Organic/Inorganic Hybrids. *J. Mater. Chem. B* **2013**, *1*, 3128−3135.

(5) Tang, F. Q.; Li, L. L.; Chen, D. Mesoporous Silica Nanoparticles: Synthesis, Biocompatibility and Drug Delivery. *Adv. Mater.* **2012**, *24*, 1504−1534.

(6) Wu, S. H.; Hung, Y.; Mou, C. Y. Mesoporous Silica Nanoparticles as Nanocarriers. *Chem. Commun.* **2011**, *47*, 9972−9985.

(7) Hudson, S. P.; Padera, R. F.; Langer, R.; Kohane, D. S. The Biocompatibility of Mesoporous Silicates. *Biomaterials* **2008**, *29*, 4045−4055.

(8) He, Q. J.; Zhang, J. M.; Shi, J. L.; Zhu, Z. Y.; Zhang, L. X.; Bu, W. B.; Guo, L. M.; Chen, Y. The Effect of PEGylation of Mesoporous Silica Nanoparticles on Nonspecific Binding of Serum Proteins and Cellular Responses. *Biomaterials* **2010**, *31*, 1085−1092.

(9) Xing, L.; Zheng, H. Q.; Cao, Y. Y.; Che, S. A. Coordination Polymer Coated Mesoporous Silica Nanoparticles for pH-responsive Drug Release. *Adv. Mater.* **2012**, *24*, 6433−6437.
(10) He, Q. J.; Gao, Y.; Zhang, L. X.; Zhang, Z. W.; Gao, F.; Ji, X. F.; Li, Y. P.; Shi, J. L. A pH-responsive Mesoporous Silica Nanoparticles-Based Multi-Drug Delivery System for Overcoming Multi-Drug Resistance. *Biomaterials* **2011**, *32*, 7711−7720.
(11) Kim, H. J.; Matsuda, H.; Zhou, H. S.; Honma, I. Ultrasound-Triggered Smart Drug Release from a Poly(dimethylsiloxane)-Mesoporous Silica Composite. *Adv. Mater.* **2006**, *18*, 3083−3088.
(12) Wang, X.; Chen, H. R.; Chen, Y.; Ma, M.; Zhang, K.; Li, F. Q.; Zheng, Y. Y.; Zeng, D. P.; Wang, Q.; Shi, J. L. Perfluorohexane-Encapsulated Mesoporous Silica Nanocapsules as Enhancement Agents for Highly Efficient High Intensity Focused Ultrasound (HIFU). *Adv. Mater.* **2012**, *24*, 785−791.
(13) Nagase, K.; Kobayashi, J.; Kikuchi, A.; Akiyama, Y.; Kanazawa, H.; Okano, T. Thermally-Modulated on/off-Adsorption Materials for Pharmaceutical Protein Purification. *Biomaterials* **2011**, *32*, 619−627.
(14) Croissant, J.; Zink, J. I. Nanovalve-Controlled Cargo Release Activated by Plasmonic Heating. *J. Am. Chem. Soc.* **2012**, *134*, 7628−7631.
(15) Mal, N. K.; Fujiwara, M.; Tanaka, Y. Photocontrolled Reversible Release of Guest Molecules from Coumarin-Modified Mesoporous Silica. *Nature* **2003**, *421*, 350−353.
(16) Liu, J. A.; Bu, W. B.; Pan, L. M.; Shi, J. L. NIR-Triggered Anticancer Drug Delivery by Upconverting Nanoparticles with Integrated Azobenzene-Modified Mesoporous Silica. *Angew. Chem., Int. Ed.* **2013**, *52*, 4375−4379.
(17) Luo, Z.; Cai, K. Y.; Hu, Y.; Zhao, L.; Liu, P.; Duan, L.; Yang, W. H. Mesoporous Silica Nanoparticles End-Capped With Collagen: Redox-Responsive Nanoreservoirs for Targeted Drug Delivery. *Angew. Chem., Int. Ed.* **2011**, *50*, 640−643.
(18) Kim, H.; Kim, S.; Park, C.; Lee, H.; Park, H. J.; Kim, C. Glutathione-Induced Intracellular Release of Guests from Mesoporous Silica Nanocontainers with Cyclodextrin Gatekeepers. *Adv. Mater.* **2010**, *22*, 4280−4283.
(19) Zhang, J.; Yuan, Z. F.; Wang, Y.; Chen, W. H.; Luo, G. F.; Cheng, S. X.; Zhuo, R. X.; Zhang, X. Z. Multifunctional Envelope-Type Mesoporous Silica Nanoparticles for Tumor-Triggered Targeting Drug Delivery. *J. Am. Chem. Soc.* **2013**, *135*, 5068−5073.
(20) Zhao, C. X.; Yu, L.; Middelberg, A. P. J. Magnetic Mesoporous Silica Nanoparticles End-Capped with Hydroxyapatite for pH-Responsive Drug Release. *J. Mater. Chem. B* **2013**, *1*, 4828−4833.
(21) Ma, M.; Chen, H. R.; Chen, Y.; Wang, X.; Chen, F.; Cui, X.; Shi, J. L. Au Capped Magnetic Core/Mesoporous Silica Shell Nanoparticles for Combined Photothermo-/Chemo-Therapy and Multimodal Imaging. *Biomaterials* **2012**, *33*, 989−998.
(22) Zhu, Y. C.; Liu, H. J.; Li, F.; Ruan, Q. C.; Wang, H.; Fujiwara, M.; Wang, L. Z.; Lu, G. Q. Dipolar Molecules as Impellers Achieving Electric-Field-Stimulated Release. *J. Am. Chem. Soc.* **2010**, *132*, 1450−1451.
(23) Coll, C.; Mondragon, L.; Martinez-Manez, R.; Sancenon, F.; Marcos, M. D.; Soto, J.; Amoros, P.; Perez-Paya, E. Enzyme-Mediated Controlled Release Systems by Anchoring Peptide Sequences on Mesoporous Silica Supports. *Angew. Chem., Int. Ed.* **2011**, *50*, 2138−2140.
(24) Popat, A.; Ross, B. P.; Liu, J.; Jambhrunkar, S.; Kleitz, F.; Qiao, S. Z. Enzyme-Responsive Controlled Release of Covalently Bound Prodrug from Functional Mesoporous Silica Nanospheres. *Angew. Chem., Int. Ed.* **2012**, *51*, 12486−12489.
(25) Mura, S.; Nicolas, J.; Couvreur, P. Stimuli-Responsive Nanocarriers for Drug Delivery. *Nat. Mater.* **2013**, *12*, 991−1003.
(26) Zhang, Q.; Liu, F.; Nguyen, K. T.; Ma, X.; Wang, X. J.; Xing, B. G.; Zhao, Y. L. Multifunctional Mesoporous Silica Nanoparticles for Cancer-Targeted and Controlled Drug Delivery. *Adv. Funct. Mater.* **2012**, *22*, 5144−5156.
(27) Zhu, Y. F.; Shi, J. L.; Shen, W. H.; Dong, X. P.; Feng, J. W.; Ruan, M. L.; Li, Y. S. Stimuli-responsive Controlled Drug Release from a Hollow Mesoporous Silica Sphere/Polyelectrolyte Multilayer Core-Shell Structure. *Angew. Chem., Int. Ed.* **2005**, *44*, 5083−5087.
(28) Singh, N.; Karambelkar, A.; Gu, L.; Lin, K.; Miller, J. S.; Chen, C. S.; Sailor, M. J.; Bhatia, S. N. Bioresponsive Mesoporous Silica Nanoparticles for Triggered Drug Release. *J. Am. Chem. Soc.* **2011**, *133*, 19582−19585.
(29) Feng, W.; Zhou, X. J.; He, C. L.; Qiu, K. X.; Nie, W.; Chen, L.; Wang, H. S.; Mo, X. M.; Zhang, Y. Z. Polyelectrolyte Multilayer Functionalized Mesoporous Silica Nanoparticles for pH-Responsive Drug Delivery: Layer Thickness-Dependent Release Profiles and Biocompatibility. *J. Mater. Chem. B* **2013**, *1*, 5886−5898.
(30) Vergaro, V.; Scarlino, F.; Bellomo, C.; Rinaldi, R.; Vergara, D.; Maffia, M.; Baldassarre, F.; Giannelli, G.; Zhang, X. C.; Lvov, Y. M.; Leporatti, S. Drug-Loaded Polyelectrolyte Microcapsules for Sustained Targeting of Cancer Cells. *Adv. Drug Delivery Rev.* **2011**, *63*, 847−864.
(31) Ariga, K.; Lvov, Y. M.; Kawakami, K.; Ji, Q.; Hill, J. P. Layer-by-Layer Self-Assembled Shells for Drug Delivery. *Adv. Drug Delivery Rev.* **2011**, *63*, 762−771.
(32) Deshmukh, P. K.; Ramani, K. P.; Singh, S. S.; Tekade, A. R.; Chatap, V. K.; Patil, G. B.; Bari, S. B. Stimuli-Sensitive Layer-by-Layer (LbL) Self-Assembly Systems: Targeting and Biosensory Applications. *J. Controlled Release* **2013**, *166*, 294−306.
(33) Li, Z. S.; Ramay, H. R.; Hauch, K. D.; Xiao, D.; Zhang, M. Q. Chitosan−Alginate Hybrid Scaffolds for Bone Tissue Engineering. *Biomaterials* **2005**, *26*, 3919−3928.
(34) Rinaudo, M. Chitin and Chitosan: Properties and Applications. *Prog. Polym. Sci.* **2006**, *31*, 603−632.
(35) Yuan, W. Y.; Dong, H.; Li, C. M.; Cui, X. Q.; Yu, L.; Lu, Z. S.; Zhou, Q. pH-Controlled Construction of Chitosan/Alginate Multilayer Film: Characterization and Application for Antibody Immobilization. *Langmuir* **2007**, *23*, 13046−13052.
(36) Zhao, Q. H.; Han, B. S.; Wang, Z. H.; Gao, C. Y.; Peng, C. H.; Shen, J. C. Hollow Chitosan-Alginate Multilayer Microcapsules as Drug Delivery Vehicle: Boxorubicin Loading and in Vitro and in Vivo studies. *Nanomed. Nanotechnol. Biol. Med.* **2007**, *3*, 63−74.
(37) Prabaharan, M.; Mano, J. F. Stimuli-Responsive Hydrogels Hased on Polysaccharides Incorporated with Thermo-Responsive Polymers as Novel Biomaterials. *Macromol. Biosci.* **2006**, *6*, 991−1008.
(38) Alves, N. M.; Mano, J. F. Chitosan Derivatives Obtained by Chemical Modifications for Biomedical and Environmental Applications. *Int. J. Biol. Macromol.* **2008**, *43*, 401−414.
(39) Zhou, J.; Romero, G.; Rojas, E.; Ma, L.; Moya, S.; Gao, C. Y. Layer by Layer Chitosan/Alginate Coatings on Poly(lactide-co-glycolide) Nanoparticles for Antifouling Protection and Folic Acid Binding to Achieve Selective Cell Targeting. *J. Colloid Interface Sci.* **2010**, *345*, 241−247.
(40) Lee, J. E.; Lee, N.; Kim, H.; Kim, J.; Choi, S. H.; Kim, J. H.; Kim, T.; Song, I. C.; Park, S. P.; Moon, W. K.; Hyeon, T. Uniform Mesoporous Dye-Doped Silica Nanoparticles Decorated with Multiple Magnetite Nanocrystals for Simultaneous Enhanced Magnetic Resonance Imaging, Fluorescence Imaging, and Drug Delivery. *J. Am. Chem. Soc.* **2010**, *132*, 552−557.
(41) Yang, Y. J.; Tao, X.; Hou, Q.; Chen, J. F. Fluorescent Mesoporous Silica Nanotubes Incorporating CdS Quantum Dots for Controlled Release of Ibuprofen. *Acta Biomater.* **2009**, *5*, 3488−3496.
(42) Rosenholm, J. M.; Sahlgren, C.; Linden, M. Towards multifunctional, Targeted Drug Delivery Systems Using Mesoporous Silica Nanoparticles - Opportunities & Challenges. *Nanoscale* **2010**, *2*, 1870−1883.
(43) Yang, C. A.; Tan, J. P. K.; Cheng, W.; Attia, A. B. E.; Ting, C. T. Y.; Nelson, A.; Hedrick, J. L.; Yang, Y. Y. Supramolecular Nanostructures Designed for High Cargo Loading Capacity and Kinetic Stability. *Nano Today* **2010**, *5*, 515−523.
(44) Zhao, Y.; Sun, X.; Zhang, G.; Trewyn, B. G.; Slowing, I. I.; Lin, V. S.-Y. Interaction of Mesoporous Silica Nanoparticles with Human Red Blood Cell Membranes: Size and Surface Effects. *ACS Nano* **2011**, *5*, 1366−1375.

(45) Ding, Y.; Zhao, Y.; Tao, X.; Zheng, Y. Z.; Chen, J. F. Assembled Alginate/Chitosan Micro-Shells for Removal of Organic Pollutants. *Polymer* **2009**, *50*, 2841−2846.
(46) Shen, H. J.; Shi, H.; Xie, M.; Ma, K.; Li, B.; Shen, S.; Wang, X. S.; Jin, Y. Biodegradable Chitosan/Alginate BSA-Gel-Capsules for pH-Controlled Loading and Release of Doxorubicin and Treatment of Pulmonary Melanoma. *J. Mater. Chem. B* **2013**, *1*, 3906−3917.
(47) Chen, J.; Qiu, X. Z.; Ouyang, J.; Kong, J. M.; Zhong, W.; Xing, M. M. pH and Reduction Dual-Sensitive Copolymeric Micelles for Intracellular Doxorubicin Delivery. *Biomacromolecules* **2011**, *12*, 3601−3611.
(48) Vallhov, H.; Gabrielsson, S.; Strømme, M.; Scheynius, A.; Garcia-Bennett, A. E. Mesoporous Silica Particles Induce Size Dependent Effects on Human Dendritic Cells. *Nano Lett.* **2007**, *7*, 3576−3582.
(49) Slowing, I. I.; Vivero-Escoto, J. L.; Wu, C. W.; Lin, V. S. Y. Mesoporous Silica Nanoparticles as Controlled Release Drug Delivery and Gene Transfection Carriers. *Adv. Drug Delivery Rev.* **2008**, *60*, 1278−1288.
(50) Han, S. Y.; Liu, Y. X.; Nie, X.; Xu, Q.; Jiao, F.; Li, W.; Zhao, Y. L.; Wu, Y.; Chen, C. Y. Efficient Delivery of Antitumor Drug to the Nuclei of Tumor Cells by Amphiphilic Biodegradable Poly(L-Aspartic Acid-co-Lactic Acid)/DPPE Co-Polymer Nanoparticles. *Small* **2012**, *8*, 1596−1606.